Microchimica Acta (2024) 191:176
https://doi.org/10.1007/s00604-024-06254-y

ORIGINAL PAPER

CTAB-Co-MOFs@AuPt NPs as signal probes for the electrochemical detection of carcinoembryonic antigen 15–3

Tingting Zhang[1] · Yan Ma[1] · Ruifen Tian[1] · Yuzhong Zhang[1]

Received: 30 November 2023 / Accepted: 1 February 2024 / Published online: 4 March 2024

Abstract

A sensitive electrochemical strategy for carcinoembryonic antigen 15–3 (CA15-3) detection is reported using CTAB-Co-MOFs@AuPt NPs as signal probes. The electrochemical strategy was designed as follows: First, the graphene aerogel@gold nanoparticles (GA@Au NPs) nanocomposites were employed to modify the sensing surface for promoting electron transfer rate and primary antibody (Ab_1) immobilization due to GA possesses a large specific surface area, eminent conductivity, and a 3D network structure. Cobalt metal–organic frameworks (CTAB-Co-MOFs) synthesized were then used as a carrier for AuPt NPs and secondary antibody (Ab_2) immobilization (notes: labelled-Ab_2). With sandwich immunoreaction, the labelled-Ab_2 was captured on the surface of the GA@Au NPs nanocomposites. Finally, differential pulse voltammetry (DPV) was employed to register the electrochemical signal of the immunosensor at the potential of − 0.85 V (vs SCE) in phosphate buffer saline (PBS) containing 2.5 mM H_2O_2. It was verified that the electrochemical reduction signal from Co^{3+} to Co^{2+} was recorded. The AuPt NPs could catalyze the reaction of H_2O_2 oxidizing Co^{2+} to Co^{3+}, resulting in the amplification of the electrochemical signal. Under the selected conditions, the immunosensor can detect CA15-3 in the range 10 μU/mL to 250 U/mL with a low detection limit of 1.1 μU/mL. In the designed strategy, the CTAB-Co-MOFs were not only employed as carriers for AuPt NPs, but also acted as signal probes. The CTAB-Co-MOFs were investigated including SEM, TEM, XPS, and XRD. The application ability of the immunosensor was evaluated using serum sample, demonstrating the immunosensor can be applied to clinic serum analysis.

Keywords Metal–organic framework · Carcinoembryonic antigen 15–3 · Au Pt nanoparticles · Electrochemical immunosensor · Differential pulse voltammetry · Signal amplification

Introduction

Breast cancer (BC) has always been one of the most significant death causes of women, and it becomes the first of cancer patient in the world according to the latest statistics from the World Health Organization [1]. As is well known, early diagnosis and treatment in time would greatly improve the survival rate of patients. Fortunately, detecting cancer biomarkers provides a new future for early diagnosis of BC. Currently, carbohydrate antigen 15–3 (CA15-3) is recognized as the most significant breast tumor markers [2], which was used to evaluate the human normal and diseased states. Usually, the serum CA15-3 levels below 30 U/mL are regarded as healthy states, and above 30 U/mL hints a high risk of BC [3]. Therefore, developing a rapid and sensitive detection technique of CA15-3 is very crucial for early diagnosis and later treatment.

Currently, the detection methods of CA15-3 biomarker have photoelectrochemical (PEC) [4], chemiluminescence [5], fluorescence [6], and enzyme-linked immunosorbent assay (ELISA) [7]. Nevertheless, the above methods suffer from complex operations, expensive equipment, and trained personnel. ELISA needs enzyme to partake, and the activity of enzyme is affected from pH and temperature, resulting in low repeatability. Hence, it is still challenging to develop a method for detecting CA15-3 with simple, sensitive, and high repeatability. Electrochemical immunosensors have been widely applied to cancer biomarkers detection owing to these virtues of sensitivity, high selectivity, quick readout, and easy to miniaturize [8–10]. For example, Feng's group [9] reported a sandwich-type electrochemical immunosensing of CYFRA 21–1 cancer marker.

✉ Yuzhong Zhang
zhyz65@mail.ahnu.edu.cn

[1] College of Chemistry and Materials Science, Anhui Key Laboratory of Chem-Biosensing, Anhui Normal University, Wuhu 241002, People's Republic of China

As is well known, cancer biomarkers in clinical samples are low abundance, in order to detect lower level of cancer biomarkers; signal amplification strategies are often introduced to augment the sensitivity of immunosensors. From the literature, nanomaterials, such as graphene and Au NPs are often employed to enhance sensing sensitivity [11]. However, the sensitivity of immunosensors reported is not high enough and lacks of real sample application. So, it is also challenging to develop higher sensitive electrochemical immunosensors to detect low abundance of serum cancer biomarkers. Recently, graphene aerogel (GA), featuring a 3D hollow network structure and rich porosity, large specific surface area, and ultra-low density [12], has been causing a great deal of attention. The GA not only inherits the good physical and chemical peculiarities of graphene [13], but also stability, ion diffusion, and electron transport rate have been improved clearly [14]. As a result, GA shows good application ability in energy storage and sensing fields [15–17].

Metal–organic frameworks (MOFs), a new type of material, have attracted extensive interest owing to their virtues of large specific surface area, adjustable porosity, abundant functional groups, and unsaturated metal sites [18, 19]. Furthermore, different functional materials or signal molecules, catalysts, and signal probes [20] can be loaded on MOFs to improve the sensitivity of sensor. For example, Guan and his coworkers [21] employed Co-MOFs as signal probes and toluidine blue (TB) as reference probes to fabricate a dual-signal ratiometric aptasensor for ochratoxin A detection. Liu and his coworkers [22] employed Ag-MOFs as signal probes to detect cancer biomarker CEA. Inspired by the advantages of MOFs and literature previously, in this work, we developed a sensitive electrochemical immunosensor for detecting the cancer biomarker CA15-3 using CTAB-Co-MOFs materials as signal probes. The designed immunosensor possesses the following advantages. Firstly, GA@Au NPs, 3D nano-network structure, high conductivity, and large specific surface area are used as a sensing matrix to amplify electrochemical signal. Secondly, CTAB-Co-MOFs not only serve as carriers for AuPt NPs and Ab_2 immobilization, but also act as signal probes. AuPt NPs have catalysis ability to the system of H_2O_2-Co^{2+}, resulting in sensing signal amplification clearly. As a result, the immunosensor demonstrated prominent performance, including good sensitivity and selectivity.

Experimental section

Chemicals, reagents, and instruments

Related chemicals, reagents, and instruments are indicated in the Supplementary Materials (Section S1 and Section S2).

Synthesis of materials

Au NPs [23], Pt NPs [24], CTAB-Co-MOFs [25], GA@Au NPs, and CTAB-Co-MOFs@AuPt NPs materials were synthesized with slight modification according to the reported literature. The related specific synthesis steps can be sought out in the Supplementary Materials (Section S3).

Preparation of labelled-Ab_2 bioconjugates

The preparation of labelled-Ab_2 bioconjugates is shown in the Supplementary Materials (Section S4).

Fabrication of the electrochemical immunosensor

The building process of the immunosensor is shown in Scheme 1. Simple, the glassy carbon electrode (GCE) was first handled by polishing, washing ultrasonically, and drying in a flow of nitrogen [26]. The following materials were sequentially assembled on the surface of GCE. Firstly, 10 μL of GA@Au NPs (1 mg/mL) suspension solution was dropped on GCE and dried in a 37 °C vacuum oven. Secondly, 6 μL of CA15-3 antibody (Ab_1, 20 μg/mL) was coated and incubated at 4 °C overnight to anchor the antibody. At each subsequent step, the modified electrode was washed with PBS (0.01 M, pH = 7.4) solution to avoid analyte adsorption on the electrode surface. Subsequently, the electrode was blocked with 6 μL bovine serum albumin solution (BSA, 1 wt%) and incubated at room temperature for 30 min. After that, 6 μL CA15-3 solution with a series of concentrations was added and incubated at 37 °C for 1 h. Finally, 6 μL of CTAB-Co-MOFs@AuPt NPs-Ab_2 solution was added dropwise on the electrode to specifically bind by antibody-antigen interactions to construct a sandwich-type immunosensor. The immunosensor was incubated at 37 °C for 1 h and stored at 4 °C when not in use.

Electrochemical measurements

Electrochemical measurements are revealed in the Supplementary Materials (Section S5).

Results and discussion

Design principle of immunosensor

GA@Au NPs were selected for sensing matrix to connect with Ab_1 vs Au-NH_2 bond. CTAB-Co-MOFs, larger specific surface area, were employed as a carrier for AuPt NPs and Ab_2 immobilization. In the presence of CA 15–3, a sandwich-type

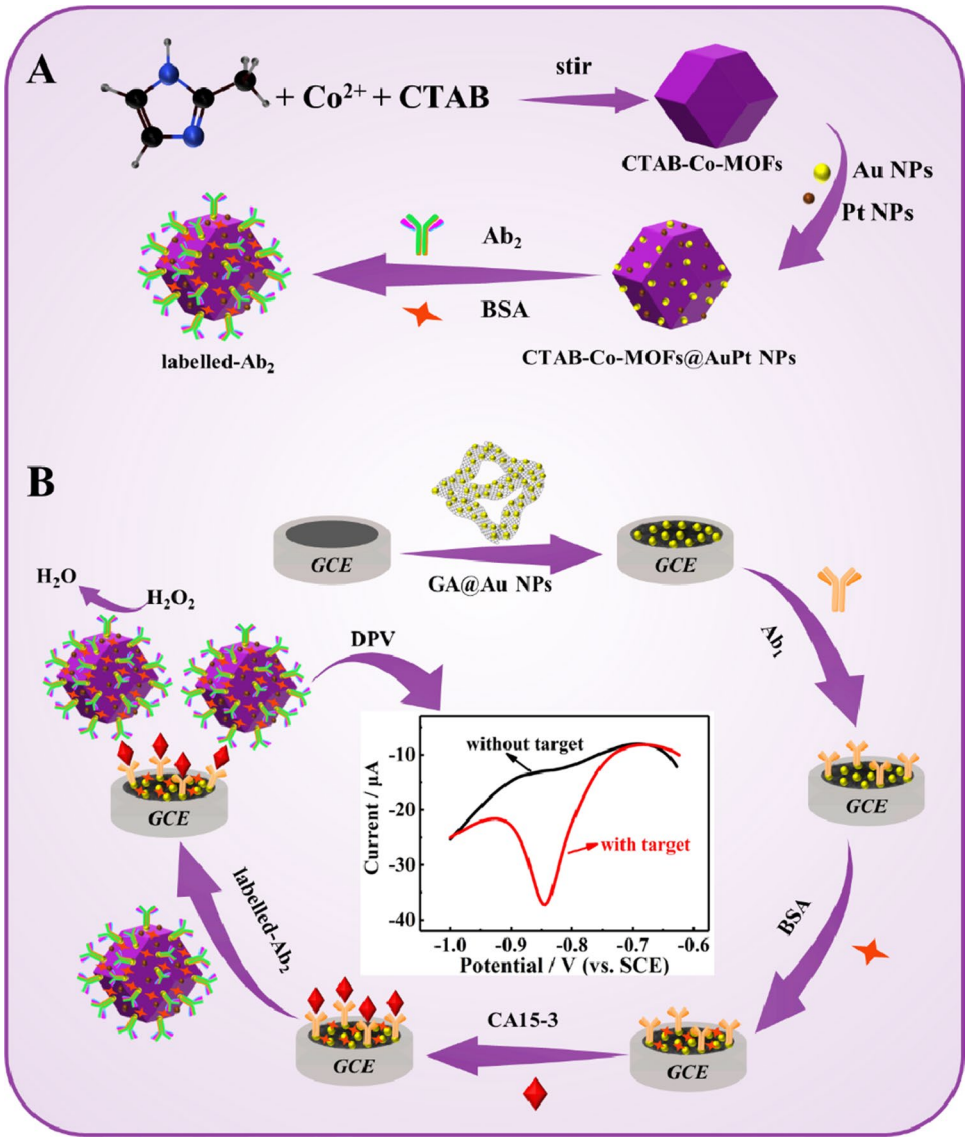

Scheme 1 Schematic diagram of the fabrication process of the immunosensor (**A** Synthesis of CTAB-Co-MOFs and labelled-Ab_2. **B** The assembling process of immunosensor)

immune complex was formed on the electrode surface by use of the specific interaction of Ab and Ag. H_2O_2 can catalyze the Co^{2+}/Co^{3+} reaction process, meanwhile, AuPt NPs on the surface of CTAB-Co-MOFs can catalyze the reaction of H_2O_2 oxidizing Co^{2+} to Co^{3+}. The electrochemical reduction response of Co^{3+}/Co^{2+} in CTAB-Co-MOFs self was used for the sensing signal. The signal intensity was related to CA15-3 level, so CA15-3 can be quantified via measuring the signal intensity change. The multiple amplification improves the sensitivity of immunosensor. The mechanism is shown as follows:

$$Co^{2+} + H_2O_2 \xrightarrow{AuPt\ NPs} Co^{3+} + H_2O + O_2$$

$$Co^{3+} + e \rightarrow Co^{2+}$$

Characterization of materials

Characterization of GA@AuNPs nanocomposites

Figure 1A and Fig. S1 show photographs and SEM images of GA at different magnifications. It can be seen that GA consists of randomly arranged and fluffy wrinkled graphene sheets and interconnected with each other to present a porous 3D network structure, which improves the stability of the material and enhances the electrical conductivity [14]. Figure 1B shows the SEM of GA @Au NPs; the Au NPs with a size of 16.72 ± 0.91 nm are consistently spread on the surface of GA, indicating that GA@Au NPs nanocomposites were successfully prepared.

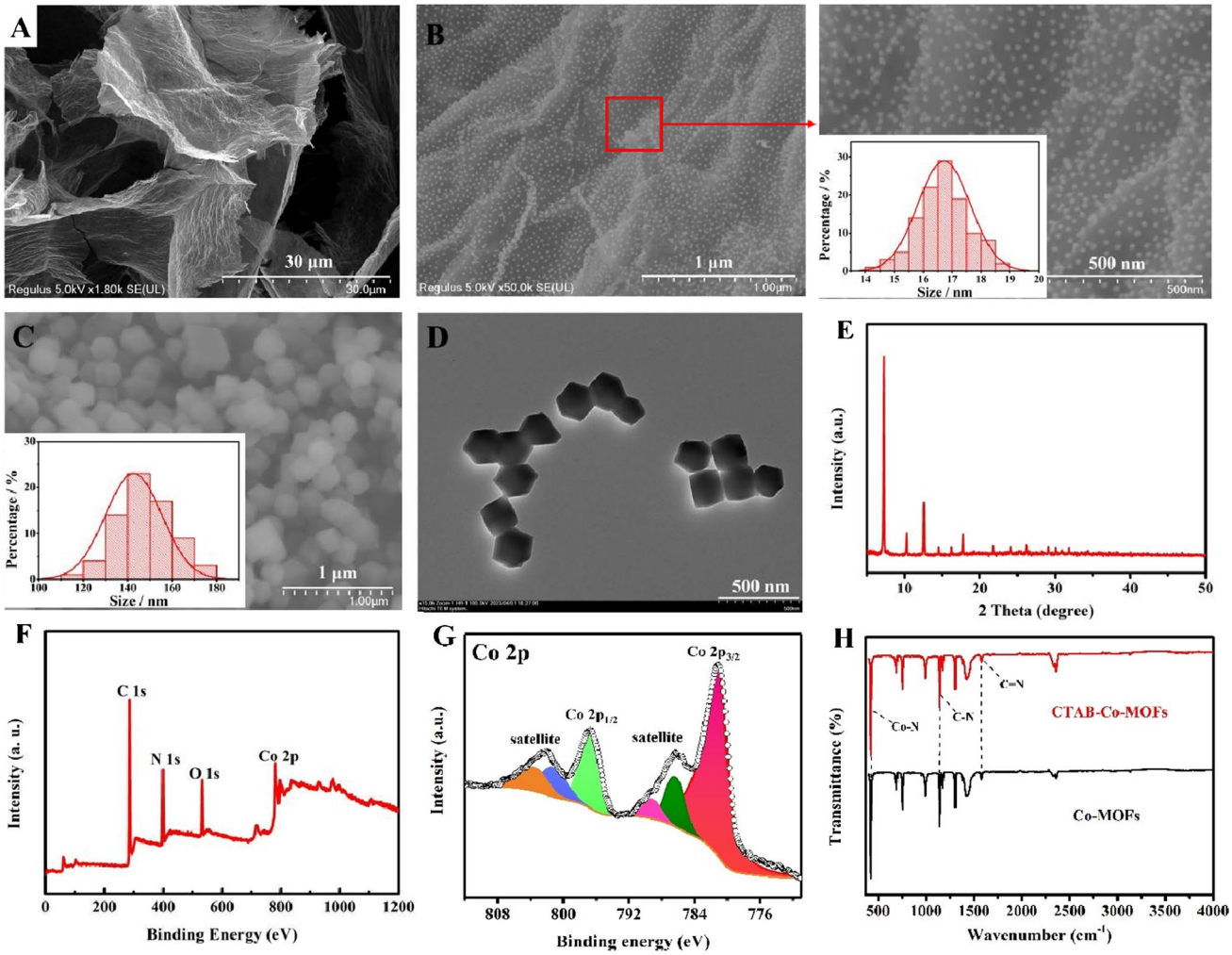

Fig. 1 **A** SEM image of GA. **B** SEM images of GA@Au NPs at different magnifications (inset size distribution). **C** SEM image of CTAB-Co-MOFs (inset size distribution), **D** TEM image of CTAB-Co-MOFs, **E** XRD, **F** XPS spectra of CTAB-Co-MOFs. **G** High-resolution XPS fitting spectra of Co 2p. **H** FT-IR patterns of CTAB-Co-MOFs and Co-MOFs

Characterization of CTAB-Co-MOFs

SEM and TEM were applied to characterize the morphology of the CTAB-Co-MOFs (Fig. 1C, D). The CTAB-Co-MOFs exhibit a regular polyhedral structure and the average size is about 142.68 ± 12.76 nm. Figure 1E shows the XRD diffraction peak of CTAB-Co-MOFs, the distinctly sharp and intense characteristic peaks at 5° to 35° indicate high crystallinity of CTAB-Co-MOFs [25]. XPS was employed to investigate the surface composition of it. It is clear that the product contains Co, C, N, and O elements (Fig. 1F), which is in accordance with the results of EDS (Fig. S2). Furthermore, the high-resolution Co 2p XPS spectra show that peaks of Co $2p_{3/2}$ and Co $2p_{1/2}$ appear at 781.18 and 796.68 eV [27], and satellite peaks emerge at 786.58 ~ 789.48 eV and 801.48 ~ 803.98 eV (Fig. 1G). The FT-IR technique was used to verify relevant functional groups in MOFs (Fig. 1H), the stretching vibration characteristic peaks of Co – N at 424.1 cm^{-1}, and C – N and C = N at 1142.3 cm^{-1} and 1579.1 cm^{-1} are observed in CTAB-Co-MOFs, respectively [27]. All investigations confirmed the successful synthesis of the CTAB-Co-MOFs.

In addition, the difference between CTAB-Co-MOFs and Co-MOFs was investigated, using SEM (Fig. S4A-B), TEM (Fig. S4C-D), FT-IR (Fig. 1H) and XRD (Fig. S5). No significant difference was observed from these figures above, indicating that CTAB could not change the morphology, functional groups, and crystal structure. What is more, CTAB-Co-MOFs have better stability than Co-MOFs (Fig. S6). This suitable explanation is that the hydrophobic cetyl chain of CTAB molecules improve the water stability of CTAB-Co-MOFs [28].

Characterization of CTAB-Co-MOFs@AuPt NPs nanocomposites

TEM was used to investigate Au NPs and Pt NPs obtained (Fig. 2A, B), and it was found that Au NPs and Pt NPs were uniformly spherical with an average size of 17.5 ± 0.78 nm and 3.90 ± 0.47 nm, respectively. From the SEM and TEM images (Fig. 2C, D), it can be seen that the Au NPs and Pt NPs appeared as small clusters on the surface of the CTAB-Co-MOFs. The CTAB-Co-MOFs@AuPt NPs also exhibit

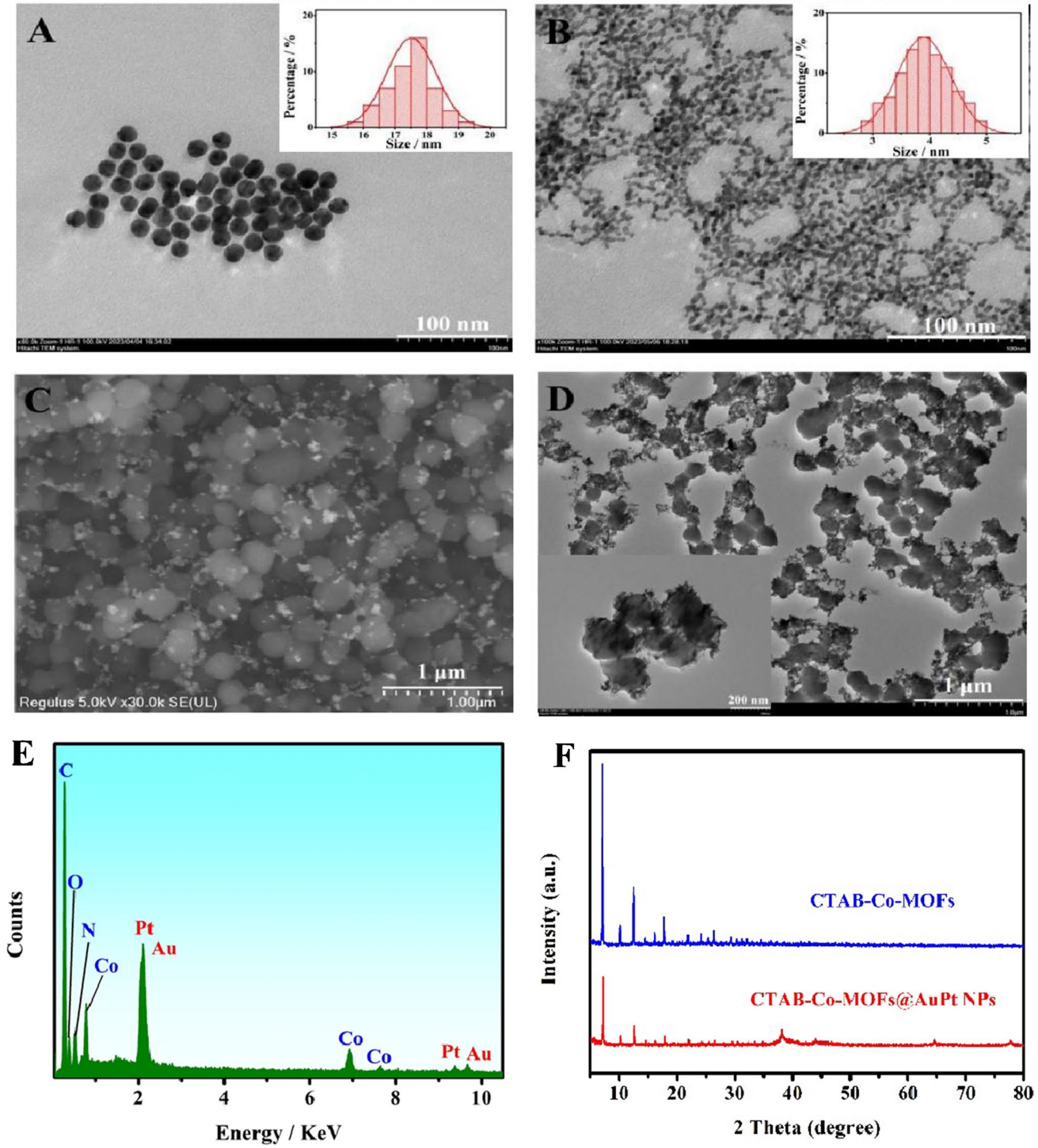

Fig. 2 TEM image with size distribution of **A** Au NPs and **B** Pt NPs. **C** SEM image, **D** TEM images and **E** EDS spectra of CTAB-Co-MOFs@AuPt NPs. **F** XRD patterns of CTAB-Co-MOFs@AuPt NPs and CTAB-Co-MOFs

the polyhedral structure similar to CTAB-Co-MOFs. Furthermore, the EDS result confirms the existence of C, N, O, Co, Au, and Pt elements (Fig. 2E). The XRD pattern displays that the CTAB-Co-MOFs@AuPt NPs composites still own an excellent crystalline state (Fig. 2F), and the AuPt NPs exhibit four characteristic peaks from 35 to 80°. Notably, the peak intensity at 38.1° is much higher than that of other planes, which manifests that Pt atoms exist in the Au matrix [29]. These results above confirm the successful preparation of CTAB-Co-MOFs@AuPt NPs.

Construction investigation of the immunosensor

Figure 3A demonstrates current density in 1.0 mM $[Fe(CN)_6]^{3-/4-}$ solution at the different stepwise process of this immunosensor. Because of the larger specific surface area and bonzer conductivity of GA@Au NPs, the GA@Au NPs/GCE (curve b) exhibited a higher current density in contrast to bare GCE (curve a). As Ab_1, BSA, CA15-3 antigen, and labelled-Ab_2 were orderly assembled on electrode surface, the current densities were reduced continuously (curves c–f) due to their nonconductivity, indicating the immunosensor was successfully prepared.

Figure 3B shows the EIS curves of 5.0 mM $[Fe(CN)_6]^{3-/4-}$ at different step of immunosensor preparation. The GA@Au NPs/GCE (curve b) presented a smaller semicircle in contrast to the bare GCE (curve a). After immobilization with Ab_1, BSA, and CA15-3 antigen, respectively, the semicircle diameter was increased sequentially (curve b–f). When labelled-Ab_2 was captured on the electrode surface, the diameter of the semicircle was further aggrandized due to antigen–antibody complex formation. The EIS results obtained were consistent with that of CV, revealing the successful manufacture of the immunosensor.

Investigation of the signal amplification and feasibility of CA15-3 analysis

In order to verify signal amplification from AuPt NPs and H_2O_2, DPV response at the same concentration of CA15-3 (100 μU/mL) was recorded for this evaluation at different conditions (seen Fig. 4A). In the absence of the labelled Ab_2 (curve a), no any signal response was observed and in the presence of CTAB-Co-MOFs@Au NPs/BSA-Ab_2, a clearly DPV signal was obtained (curve b) due to a sandwich structure formation. If the support electrolyte containing H_2O_2, the increasing DPV signal was obtained clearly (curve c), when AuPt NPs existed (curve d), the DPV signal was further increased, indicating that AuPt NPs had good catalytic ability to the system of H_2O_2—Co^{2+}.

The feasibility of CA15-3 analysis was investigated, and the results are presented in Fig. 4B. In the absence of CA15-3 (curve a), no obvious response signal was received; however, a larger response signal was obtained when existed CA15-3 (curve b). The signal intensity was related to the concentration of CA15-3. Thus, the concentration of CA15-3 can be quantified based on the peak current intensity changes, indicating the feasibility of immunosensor to detect the serum CA15-3.

Optimization of experimental condition

Herein, experimental conditions (e.g., pH, incubation temperature and time, and the concentration of Ab_1) were optimized to improve the analytical performance of the

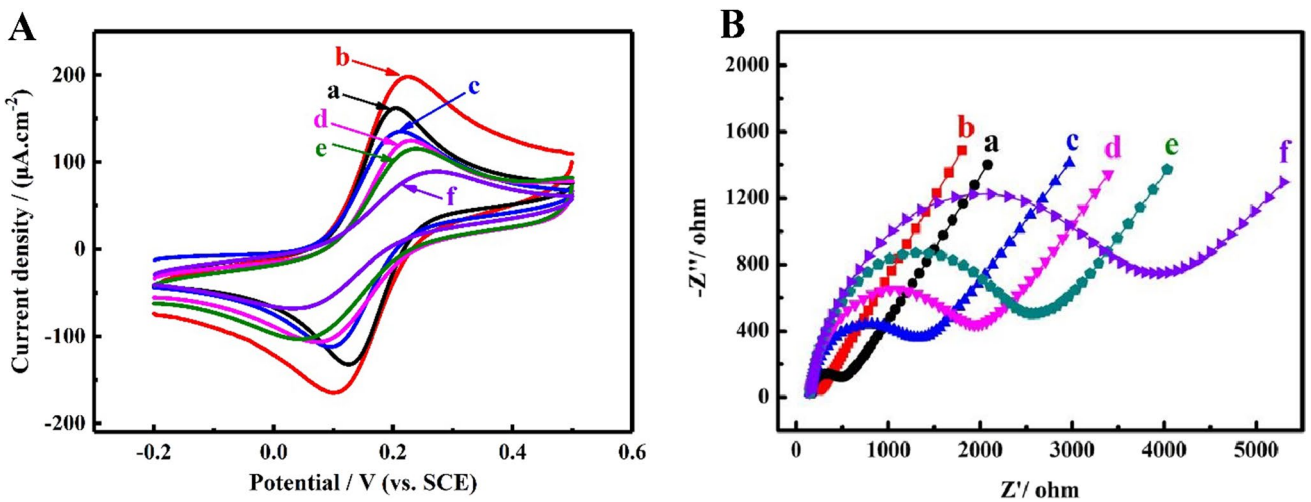

Fig. 3 **A** Current density and **B** EIS curves recorded at different modified electrodes: (a) bare GCE, (b) GA@Au NPs/GCE, (c) Ab_1/GA@Au NPs/GCE, (d) BSA/Ab_1/GA@Au NPs/GCE, (e) CA15-3/BSA/Ab_1/GA@Au NPs/GCE, (f) labelled-Ab_2/CA15-3/BSA/Ab_1/GA@Au NPs/GCE

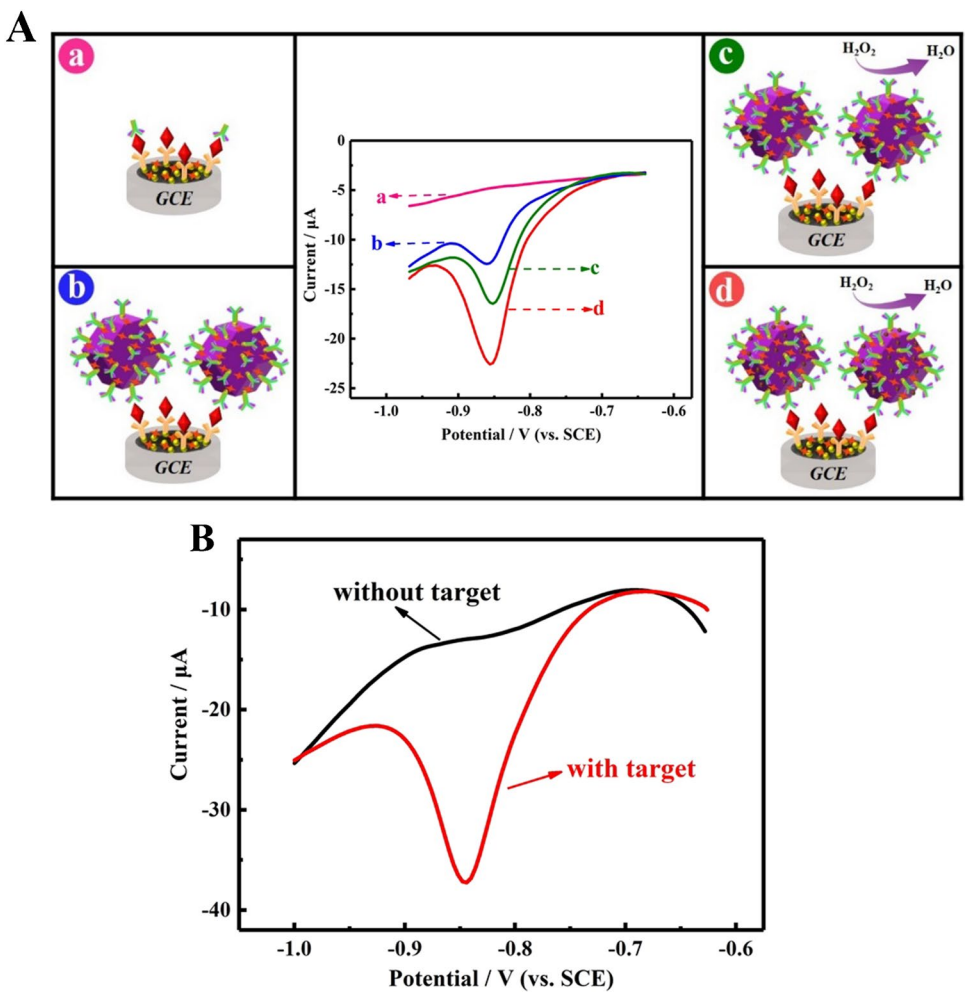

Fig. 4 **A** DPV responses of immunosensors recorded at different signal probes. (a) No labelled Ab_2 probe; (b) CTAB-Co-MOFs@Au NPs-Ab_2 probe; (c) CTAB-Co-MOFs@Au NPs-Ab_2 probe in the presence of H_2O_2; (d) CTAB-Co-MOFs@AuPt NPs-Ab_2 probe in the presence of H_2O_2. Condition: The concentration of CA15-3 is 100 μU/mL, incubation time of 60 min. **B** DPV response of the immunosensor recorded in the absence of CA15-3 antigen (curve a) and in the presence of CA15-3 antigen (curve b). Condition: The concentration of CA15-3 is 10 mU/mL, incubation time of 60 min

immunosensor. The results obtained are shown in the Supplementary Materials (Section S8). Briefly speaking, the optimized results are listed as follows: pH 7.4; incubation temperature, 37 °C; incubation time, 60 min; the concentration of Ab_1, 20 μg/mL; and the concentration of H_2O_2, 2.5 mM, and the amount of GA@Au NPs, 10 μL.

Analytical performance

Under the optimal conditions, the designed immunosensor was employed to detect different concentrations of CA15-3 and recorded their DPV response. As shown in Fig. 5A, the currents are increased gradually at the potential about − 0.85 V (vs SCE) with the increase of CA15-3 concentration, and a good working cure was obtained in the range of 10 μU/mL to 250 U/mL (Fig. 5B) with the limit of detection (LOD) was 1.1 μU/mL (at the 3σ/S, σ is the standard deviation of the blank and S is the slope of the analytical curve). The linear regression equation was $y = 4.4500 + 3.9063$ lg x (y is the peak current value (μA), x is the concentration of CA15-3 (μU/mL), $R^2 = 0.999$). Compared with other immunosensors reported previously (shown in Table 1), the immunosensor shows a wider linear range and lower LOD. The reasons of good performance can be explained as follows: (1) GA@Au NPs, good conductivity and larger surface area, were employed for sensing matrix to enhance electron transfer rate. (2) CTAB-Co-MOFs, larger specific surface area, were employed as a carrier for improving the amount of AuPt NPs and Ab_2. (3) AuPt NPs catalyze the reaction of H_2O_2 oxidizing Co^{2+} to Co^{3+}, resulting in the significant amplification of the sensing signal.

Selectivity, reproducibility, and stability

To assess the selectivity of the immunosensor, some interferences (e.g., CA19-9, IgG, PSA, HGB, HSA, Mb, and BSA) were selected for this investigation. Specifically, the immunosensor was employed to detect 0.01 U/mL CA15-3 antigen in the presence of single interfering substance and recorded DPV response corresponding to different conditions. As shown in Fig. 6A, no apparent current change was observed, hinting at the good selectivity of immunosensor.

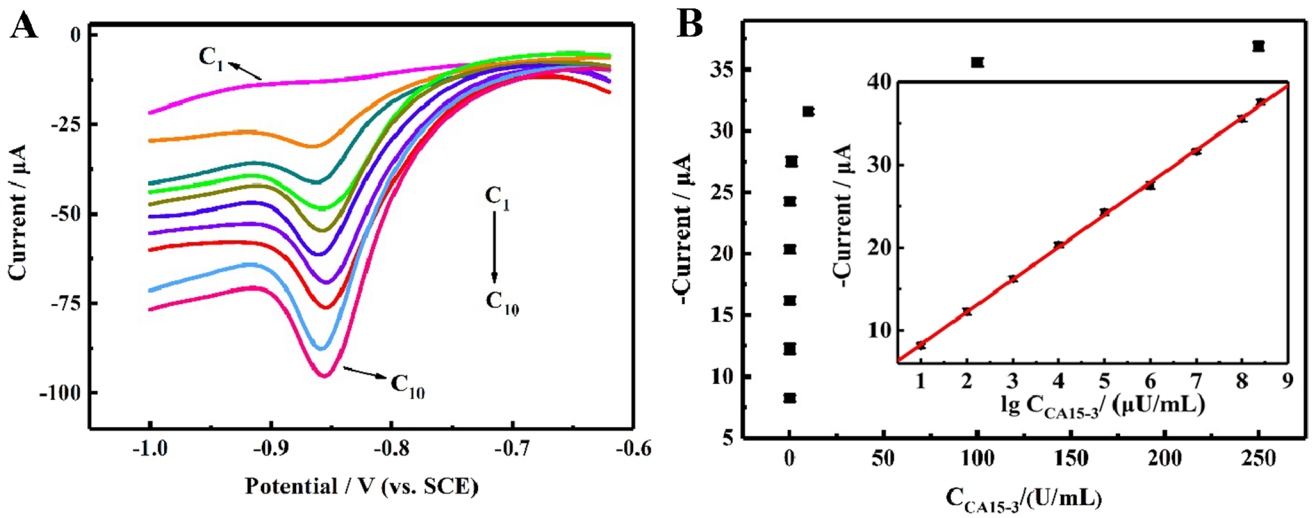

Fig. 5 **A** DPV response recorded at various CA15-3 concentrations. **B** The working curves of peak current (I) vs the logarithmic of CA15-3 concentration. Conditions (U/mL): C_1, 0; C_2, 0.00001; C_3, 0.0001; C_4, 0.001; C_5, 0.01; C_6, 0.1; C_7, 1; C_8, 10; C_9, 100; C_{10}, 250. The datum dot is average value of three times

Table 1 Comparison of CA15-3 detection with different analytical techniques

Analytical techniques	Immunosensing mode	Linear range (U/mL)	LOD (U/mL)	Human serum samples	Enzyme	Ref
PEC	Sandwich type	1×10^{-5} – 10	3.78×10^{-6}	Dilute	–	[4]
ECL	Sandwich type	0.1 – 120	0.033	Dilute	–	[5]
FL	Label-free	2.56×10^{-5} – 1.28	2.56×10^{-5}	Dilute	–	[6]
DPV	Label-free	0.1 – 200	0.0114	Dilute	–	[8]
ECL	Sandwich type	0.0005 – 500	0.0002	Dilute	–	[30]
DPV	Label-free	0.5 – 200	0.17	Dilute	–	[31]
DPV	Sandwich type	1×10^{-5} – 250	1.1×10^{-6}	Dilute	–	This method

DPV differential pulse voltammetry, *ECL* electrochemiluminescence, *PEC* photoelectrochemical, *FL* fluorescence

Reproducibility was evaluated using six immunosensors to detect CA15-3 (0.1 U/mL) under the same conditions and record their DPV response (shown in Fig. 6B). The relative standard deviation (RSD) is 0.35%. Additionally, the stability of the immunosensor was assessed by depositing it in the refrigerator (4 °C) for 7 days and testing it once a day. The results are presented in Fig. 6C, and it can be seen that the current retained 94.7% of its initial value on the 7th day, indicating the good stability of the immunosensor.

Serum sample analysis

To verify the feasibility of the proposed immunosensor, human serum sample was employed and the recovery test was adopted. According to the method described in this experiment, the sample was parallelly detected five times. The results are shown in Table 2 according to the equation ($\bar{x} \pm t\frac{s}{\sqrt{n}}$, s is the standard deviation). The recoveries obtained are within 98.33 to 102.08% with RSD values within 2.49 to 2.67%, indicating that the proposed immunosensor has good feasibility in clinical analysis.

Conclusion

In this work, a sensitive sandwich electrochemical CA15-3 immunosensor was developed using GA@Au NPs and CTAB-Co-MOFs@AuPt NPs. The proposed

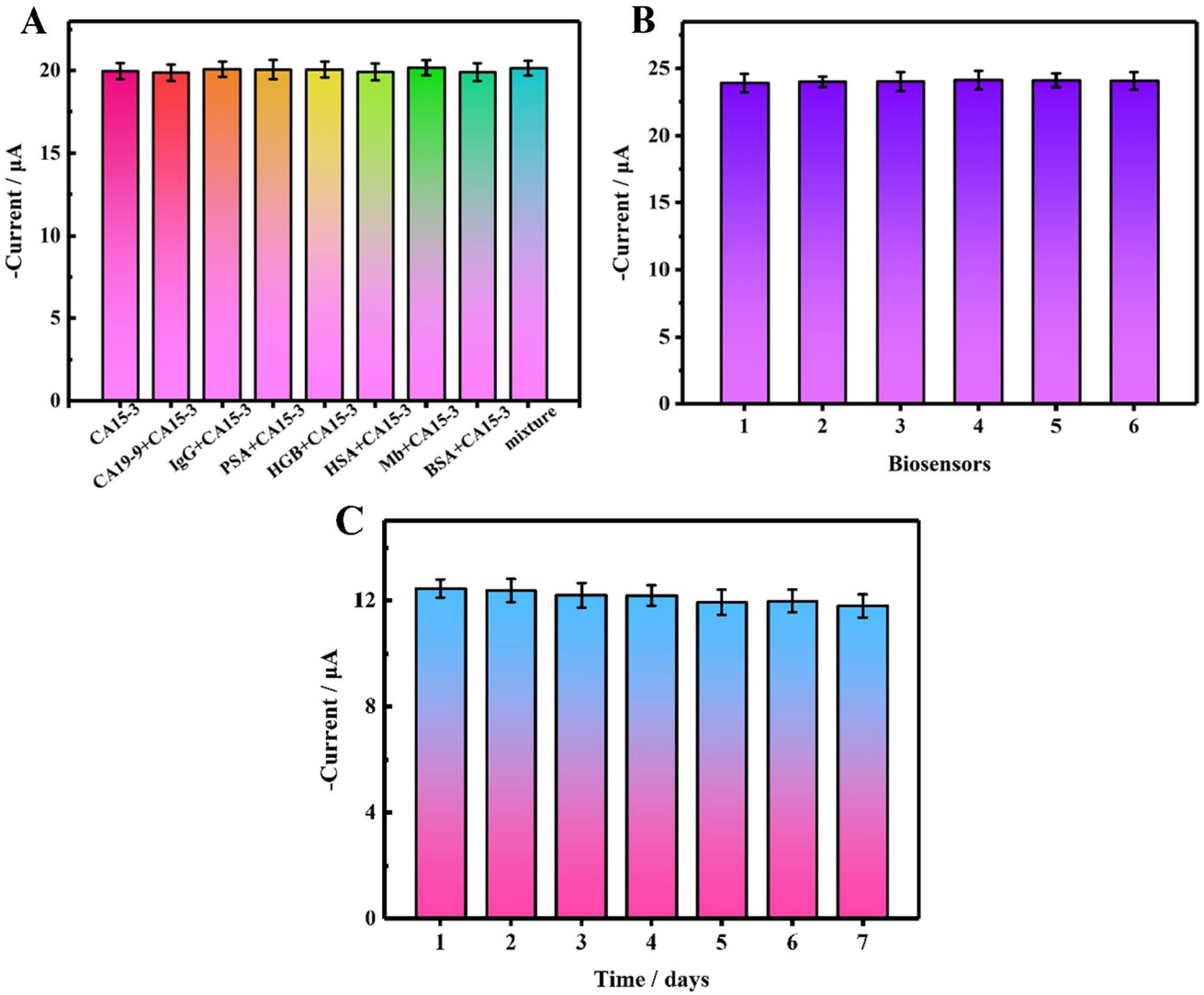

Fig. 6 **A** Specificity of the immunosensor (condition: 0.01 U/mL CA15-3; interference substances: 1 U/mL CA19-9, 10 μg/mL IgG, 10 μg/mL PSA, 100 μg/mL HGB, 100 μg/mL HSA, 100 μg/mL Mb and 100 μg/mL BSA; $n=3$). **B** Reproducibility of the immunosensor (0.1 U/mL CA15-3; $n=3$); **C** Stability of the immunosensor (100 μU/mL CA15-3; $n=3$)

Table 2 Analytical results in the human serum sample ($P=0.95$; $n=5$)

Samples	Added (U/mL)	Found (U/mL)	RSD (%)	Recovery (%)
1	1	1.021 ± 0.0339	2.67	102.08
2	0.1	0.0987 ± 0.00306	2.49	98.66
3	0.01	0.00983 ± 0.000313	2.56	98.33

immunosensor shows excellent analytical performance, including wider linear range (10 μU/mL to 250 U/mL) and lower LOD of 1.1 μU/mL. Satisfactory, the immunosensor has potential application in the early clinical diagnosis of BC via clinical serum analysis. Furthermore, the immunosensor also provides a feasible strategy for detecting other cancer biomarkers only adjust corresponding to antibody.

Supplementary Information The online version contains supplementary material available at https://doi.org/10.1007/s00604-024-06254-y.

Funding This work is supported by the Nature Science Foundation of the Education Department of Anhui Province (No KJ2016A848).

Declarations

Ethics approval All experiments were performed in accordance with the relevant laws and institutional guidelines of China, and approved by the ethics committee at Anhui Normal University (AHNU-ET2023051).

Conflict of interest The authors declare no competing interests.

References

1. Sung H, Ferlay J, Siegel RL, Laversanne M, Soerjomataram I, Jemal A, Bray F (2021) Global Cancer Statistics 2020: GLOBOCAN estimates of incidence and mortality worldwide for 36 cancers in 185 countries. CA A Cancer J Clin 71(3):209–249
2. Xiong X, Zhang Y, Wang YF, Sha HF, Jia NQ (2019) One-step electrochemiluminescence immunoassay for BC biomarker CA 15–3 based on Ru(bpy)$_6^{2+}$-coated UiO-66-NH_2 metal-organic framework. Sens Actuat B Chem 297:126812
3. Ribeiro JA, Sales MGF, Pereira CM (2021) Electrochemistry-assisted surface plasmon resonance biosensor for detection of CA 15–3. Anal Chem 93(22):7815–7824
4. Peng MX, Lin SY, Lin ZB, Zheng DL, Song YB, Lu FS, Chen YW, Gao WH (2022) Rationally constructed ZnCdS-HDCs@In_2S_3-HNRs double-hollow heterojunction with promoted light capture capability for photoelectrochemical biosensing. Biosens Bioelectron 201:113957
5. Jiang XY, Wang HJ, Yuan R, Chai YQ (2015) Sensitive electrochemiluminescence detection for CA15-3 based on immobilizing luminol on dendrimer functionalized ZnO nanorods. Biosens Bioelectron 63:33–38
6. Wu YW, Chen XL, Wang XF, Yang M, Xu FL, Hou CJ, Huo DQ (2021) A fluorescent biosensor based on prismatic hollow Metal-polydopamine frameworks and 6-carboxyfluorescein (FAM)-labeled protein aptamer for CA15-3 detection. Sensors Actuat B-Chem 329:129249
7. Ambrosi A, Airo F, Merkoci A (2010) Enhanced gold nanoparticle based ELISA for a BC biomarker. Anal Chem 82(3):1151–1156
8. Ge XY, Feng YG, Cen SY, Wang AJ, Mei LP, Luo XL, Feng JJ (2021) A label-free electrochemical immnunosensor based on signal magnification of oxygen reduction reaction catalyzed by uniform PtCo nanodendrites for highly sensitive detection of carbohydrate antigen 15–3. Anal Chim Acta 1176:338750
9. Feng YG, He JW, Chen DN, Jiang LY, Wang AJ, Bao N, Feng JJ (2022) A sandwich-type electrochemical immunosensor for CYFRA 21–1 based on probe-confined in PtPd/polydopamine/hollow carbon spheres coupled with dendritic Au@Rh nanocrystals. Microchim Acta 189:271
10. Thangapandi K, Arumugam S, Amalesh N, Ajeet K, Saikat K (2021) Bio-nanocomposite based highly sensitive and label-free electrochemical immunosensor for endometriosis diagnosticsapplication. Bioelectrochemistry 139:107740–107749
11. Jin H, Mo K, Wen F, Li Y (2019) Preparation and pervaporation performance of CAU-10-H MOF membranes. J Membrane Sci 577:129–136
12. Zhi D, Li T, Li J, Ren H, Meng F (2021) A review of three-dimensional graphene-based aerogels: Synthesis, structure and application for microwave absorption. Compos Part B-Eng 211:108642
13. Sahoo BB, Kumar N, Panda HS, Panigrahy B, Sahoo NK, Soam A, Mahanto BS, Sahoo PK (2021) Self-assembled 3D graphene-based aerogel with Au nanoparticles as high-performance supercapacitor electrode. J Energy Storage 43:103157
14. Santos-Gómez LD, García JR, Montes-Morán MA, Menéndez JA, García-Granda S, Arenillas A (2021) Ultralight-weight graphene aerogels with extremely high electrical conductivity. Small 17(41):2103407
15. Liu XT, Pang K, Yang H, Guo XZ (2020) Intrinsically microstructured graphene aerogel exhibiting excellent mechanical performance and super-high adsorption capacity. Carbon 161:146–152
16. Maleki H (2016) Recent advances in aerogels for environmental remediation applications: A review. Chem Eng J 300:98–118
17. Öner E, Öztürk A, Yurtcan AB (2020) Utilization of the graphene aerogel as PEM fuel cell catalyst support: effect of polypyrrole (PPy) and polydimethylsiloxane (PDMS) addition. Int J Hydrogen Energy 45:34818–34836
18. Indra A, Song T, Paik U (2018) Metal organic framework derived materials: progress and prospects for the energy conversion and storage. Adv Mater 30:1705146
19. Li Z, Xi Y, Zhao A, Jiang J, Li B, Yang X, He J, Li F (2021) Cobalt-imidazole metal-organic framework loaded with luminol for paper-based chemiluminescence detection of catechol with use of a smartphone. Anal Bioanal Chem 413(13):3541–3550
20. Liu SY, Lai C, Liu XG, Li BS, Zhang C, Qin L, Huang DL, Yi H, Zhang MM, Li L, Wang WJ, Zhou XR, Chen L (2020) Metal-organic frameworks and their derivatives as signal amplification elements for electrochemical sensing. Coordin Chem Rev 424:213520
21. Guan Y, Si PB, Yang T, Wu Y, Yang TH, Hu R (2023) A novel method for detection of ochratoxin A in foods—Co-MOFs based dual signal ratiometric electrochemical aptamer sensor coupled with DNA walker. Food Chem 403:134316
22. Liu JB, Shang YH, Zhu QY, Zhang XX, Zheng JB (2019) A voltammetric immunoassay for the carcinoembryonic antigen using silver(I)-terephthalate metal-organic frameworks containing gold nanoparticles as a signal probe. Microchim Acta 186:509
23. Li MY, Zhang TT, Zhang YZ (2023) Ultrasensitive electrochemical sensing platform for miRNA-21 detection based on manganese dioxide-gold nanoparticle nanoconjugates coupled with hybridization chain reaction and horseradish peroxidase signal amplification. Analyst 148(9):2180–2188
24. Liu JB, Fu SH, Yuan B, Li YL, Deng ZX (2010) Toward a universal "adhesive nanosheet" for the assembly of multiple nanoparticles based on a protein-induced reduction/decoration of graphene oxide. J Am Chem Soc 132(21):7279–7281
25. Zhu XF, Yuan S, Ju SY, Yang J, Zhao C, Liu H (2019) Water splitting-assisted electrocatalytic oxidation of glucose with a metal-organic framework for wearable nonenzymatic perspiration sensing. Anal Chem 91(16):10764–10771
26. Zhang TT, Ma Y, Zhang YZ (2023) A simple electrochemical strategy for the detection of the cancer marker CA19-9 by signal amplification using copper organic framework nanocomposite. Analyst 148(23):5905–5914
27. Zhang LX, Xian JX, Xiang XX, Ouyang H, Wang L, Fu ZF (2022) Surfactant-assisted synthesis of water-stable cobalt-imidazole

metal organic frameworks as signal probes for chemiluminescent immunoassay. Sensors Actuat B-Chem 373:132774
28. Huang Q, Guo Y, Chen D, Zhang L, Li TT, Hu Y, Qian J, Huang S (2021) Rational construction of ultrafine noble metals onto carbon nanoribbons with efficient oxygen reduction in practical alkaline fuel cell. Chem Eng J 424:130336
29. Oladipo AO, Iku SII, Ntwasa M, Nkambule TTI, Mamba BB, Msagati TAM (2020) Doxorubicin conjugated hydrophilic AuPt bimetallic nanoparticles fabricated from phragmites australis: characterization and cytotoxic activity against human cancer cells. J Drug Deliv Sci Technol 57:101749
30. Ke H, Zhang X, Huang CS, Jia NQ (2018) Electrochemiluminescence evaluation for carbohydrate antigen 15–3 based on the dual-amplification of ferrocene derivative and Pt/BSA core/shell nanospheres. Biosens Bioelectron 103:62–68
31. Wang AJ, Zhu XY, Chen Y, Luo XL, Xue YD, Feng JJ (2019) Ultrasensitive label-free electrochemical immunoassay of carbohydrate antigen 15–3 using dendritic Au@Pt nanocrystals/ferrocene-grafted-chitosan for efficient signal amplification. Sens Actuators B, Chem 292:164–170